

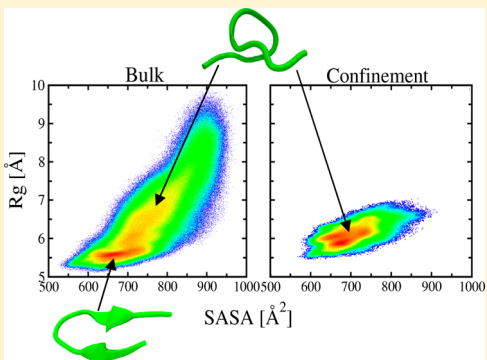
Effects of Confinement on the Structure and Dynamics of an Intrinsically Disordered Peptide: A Molecular-Dynamics Study

J. Srinivasa Rao and Luis Cruz*

Department of Physics, 3141 Chestnut Street, Drexel University, Philadelphia, Pennsylvania 19104, United States

Supporting Information

ABSTRACT: In vivo, proteins and peptides are exposed to radically different environments than those in bulk. Because of the abundance of other cellular components, proteins perform their function in crowded and confined spaces. Confinement has been shown to alter the structure, dynamics, and folding of proteins that possess a native fold. Little is known, however, of the effects of confinement on biologically important intrinsically disordered proteins or peptides (IDP). Here, we use extensive molecular dynamics simulations to investigate the effects of confinement in an IDP, the $A\beta_{21-30}$, a central folding nucleus of the full length amyloid β -protein. In this study, we report results derived from 107 μ s of molecular dynamics simulations that subjected the $A\beta_{21-30}$ to two types of confinement: hydrophilic and hydrophobic pores. Results show that turn structures are enhanced as a function of decreasing pore size (increasing confinement) over other structures, including coils, β -hairpins, and bridges. However, the percentage occurrence of the dominant hydrogen bond between amino acids Asp23 and Ser26 shown to stabilize the turn in bulk simulations does not increase as a function of confinement signifying a disconnect between structure and internal hydrogen bonding. Differences in structure and dynamics of the decapeptide due to hydrophilic and hydrophobic confinement are more apparent at the extreme confinement conditions, where a reduction of the available phase space in hydrophilic confinement is explained in terms of interactions between the decapeptide and a layer of water at the interface between the decapeptide and the surface of the pore, and a smaller size of the decapeptide in the hydrophobic pores is rationalized in terms of peptide–surface interactions.



INTRODUCTION

Protein folding in cellular environments is a problem that continues to elude detailed understanding even after several decades of continued consideration.¹ In vivo, proteins perform their biological functions by folding into their native states within cellular environments that include conditions of excluded volumes, in the presence of lipid membranes and chaperons, and within cavities, among many other conditions. In vitro, it has been shown that confinement has an intrinsic effect on protein folding.^{2–6} A typical simplifying assumption in computational and many experimental studies of the folding and aggregation of proteins has been to consider proteins in the absence of these conditions or in bulk environments. Although a necessary simplification to a very complex problem, bulk environments are far from the in vivo restricted or modified environments in which proteins exist. Recent computational^{7–31} and theoretical^{1,16,32–43} studies addressing this problem considered the effects of confinement on protein folding and stability in the context of chaperons, pores, and other cellular environments. The common observation from most of these studies was that confinement could stabilize the folded state of proteins.^{9,11,36,37,40–42} This was phenomenologically understood in terms of simple polymer models that suggested that the effects of confinement were reflected in a reduction of the conformational entropy associated with

protein folding, which in turn led to the stabilization of the folded states, consistent with experiments.^{5,44} Moreover, because these studies used different techniques and assumptions, their support for this confinement-driven enhanced protein stability suggested that this effect could be general. For example, using off-lattice Gō model, Thirumalai and Klimov showed that proteins in cavities were stabilized by reducing the entropy of the denatured ensemble,^{18,45} while Zhou and Dill using polymer physics-based models argued that proteins were stabilized in their folded states within pores.^{1,40,42,43} However, simplified coarse-grained bead models using implicit solvent that showed that β -hairpin and small protein structures were stabilized by moderate confinement also showed that they were unexpectedly destabilized in the limiting case of overconfinement.^{18,40}

A natural question is whether models can safely ignore the role that the solvent may play in these phenomena. At first glance, one would expect that confinement acts on the solvent just as it does on the protein. This effect might then be reflected on the protein as the solvent may behave differently under confinement as well as also mediate possible interactions

Received: October 26, 2012

Revised: March 11, 2013

Published: March 14, 2013

between the surface of the confining wall and the protein. To investigate the role of the solvent, Lucent et al. studied protein folding under confinement by selectively confining the protein in one case and protein and solvent in another case.⁴⁶ They showed that when only the protein was confined the folded states were stabilized because the unfolded states were destabilized. However, when both protein and solvent were confined together, the system destabilized the folded (or native) states. This result indicated that a confined solvent played an important and nontrivial role in the folding dynamics of the protein.⁴⁶ Following this study, Pande and co-workers showed computationally that when considering an explicit water–protein system, the protein folding kinetics and thermodynamics were strongly influenced by the solvent under confinement.^{12,19,47} In particular, they showed that while a confined solvent altered the overall folding mechanism of chaperons, it may not have been driving the folding.¹²

While these studies were key in exposing the importance of the explicit consideration of the solvent in confined system simulations, they were not exhaustive in terms of examining the relationship between the radius of the confined cavity and the folding behavior of proteins. Also, to some extent these studies mostly ignored the effects of the internal surface (hydrophobic/hydrophilic) on the folding and the stability of proteins. These considerations are important as other computational studies of water in confined geometries^{47–59} showed that the behavior of water near hydrophobic walls and/or surfaces exhibited properties that were different than in the bulk. Additionally, these studies also showed that confinement could distort the hydrogen bonding network, which indicated that under extreme confinement (very small cavities) the effect of hydrogen bonding could be abolished.^{49–51} A recent study by Tian et al.²³ addressed the confinement of Trp cage protein under polar and nonpolar confinement inside a fixed 2 nm in radius fullerene and showed that protein folding stability was influenced by several factors, such as the type of confined wall, sequence of the protein, and entropic stabilization. Specifically, they found that the nonpolar confinement stabilized the folded state while the polar confinement destabilized the protein due to interactions between charged side chains and the confined wall.

Here, we focus on the role of confinement on an intrinsically disordered peptide (IDP). It has been shown that many IDPs are able to perform important biological function.^{60–66} Yet, their lack of a folded structure makes them hard to characterize, specifically in the confined spaces found in the cell. In this work, we investigate the effect of confinement on the dynamics of a short IDP by varying the radius of the confining pore composed of hydrophobic and hydrophilic rough surfaces. The results are derived from exhaustive all-atom molecular dynamics (MD) simulations with explicit solvent. This peptide is a central short fragment of the amyloid β -protein ($A\beta$), the $A\beta_{21–30}$. The full-length $A\beta$, widely implicated in Alzheimer's disease (AD),^{65,67–71} has been shown to exhibit a wide range of structural and dynamical behavior typically associated with IDPs.⁶⁵ The short $A\beta_{21–30}$ fragment preserves many of the properties of the full-length peptide such as containing the folding nucleus,⁷² while avoiding the tendency to aggregate that makes experimental studies difficult,^{73,74} a characteristic that also makes the study of other fragments of $A\beta$ appealing.^{75–80} In addition, the $A\beta_{21–30}$ fragment does not have a folded state, thus behaving as an IDP.^{69,72,80,81} The data presented below underline the importance of explicitly considering the solvent

and the hydrophobicity of the confining surface in confined geometries. The results also show that even with the lack of a folded state, understanding the dynamics of the $A\beta_{21–30}$ is important and has applicability in understanding the behavior of proteins in confinement as some of the results using this IDP have a correspondence to known behavior of confined proteins.

METHODS

MD Simulations. Long-time all-atom molecular dynamics trajectories of a monomeric $A\beta_{21–30}$ in explicit TIP4P⁸² water using the OPLS/AA⁸³ force field and the GROMACS 4.0.5 package^{84,85} were performed. The amino acids of $A\beta_{21–30}$ were numbered sequentially starting from Ala21 through Ala30, corresponding to positions 21 through 30 of the full-length protein. $A\beta_{21–30}$ had the primary sequence Ala-Glu-Asp-Val-Gly-Ser-Asn-Lys-Gly-Ala, where Glu22 and Asp23 were negatively charged and Lys28 was positively charged. The N- and C-terminii of $A\beta_{21–30}$ were capped with acetyl and amide groups, respectively. In all of the trajectories analyzed here, the initial conformations of the decapeptide were chosen to belong to random coil conformations without any trace of secondary structure.

Confined systems consisted of the $A\beta_{21–30}$ and water contained in a spherical pore of radius R (R in the range from 12 to 24 Å) formed inside a larger immobile matrix of atoms or molecules in a box of side L ($L > 2R$). Hydrophilic and hydrophobic pore inner surfaces were obtained by using as the immobile matrix water molecules and argon atoms, respectively. For simplicity of calculation, periodic boundary conditions were used taking the precaution that distances between atoms inside the pores and their images were large enough such that interactions between them were negligible. The size of the system was taken to be $L = 2R + 20$ Å ($R = 12–24$ Å) in which the surface of the pore was set to be 10 Å from the boundary of the box. For the range of radii used in this work, L ranged from 44 to 68 Å.

All of the trajectories were generated using the NVT ensemble at a constant temperature of $T = 283$ K.^{72,80} This temperature was chosen to correspond to experimental work on this decapeptide⁷² and to compare results with previous computational work of this decapeptide in bulk water.⁸⁶ The temperature was controlled by coupling the system to an external bath.⁸⁷ The SETTLE algorithm was used to hold fixed the covalent bonds of the water molecules.⁸⁸ Bonds involving hydrogens were constrained according to the LINCS protocol.⁸⁹ Neighbor lists updated every 10 simulation steps were used for the nonbonded interactions. To calculate the electrostatic interactions a Particle Mesh Ewald method⁹⁰ was used with a cutoff distance of 10 Å for nonbonded interactions and a 1.2 Å grid spacing for the Fourier transform in the reciprocal space for all trajectories. To speed up simulations, a time step of 4 fs (facilitated by GROMACS) was used for all hydrophilic (fixed water pore) trajectories. However, because of sporadic sudden simulation instabilities, trajectories would stop and had to be manually restarted. Thus for convenience, but at the expense of longer simulation times, simulations for the hydrophobic (fixed argon) trajectories used a 2 fs time step that did not exhibit these instabilities and would run to the end without interruption. We independently verified that trajectories using the 4 and 2 fs time steps gave equivalent results on the relevant quantities used here.

System Setup. The procedure to generate the confined systems was the following. First, an $A\beta_{21–30}$ monomer was

inserted at the center of a box containing TIP4P water molecules by deleting all water molecules overlapping or in close proximity ($<2.4 \text{ \AA}$) to any atom of the $\text{A}\beta_{21-30}$. Then, the energy of the $\text{A}\beta_{21-30}$ and water molecules was minimized for 20 000 steps by applying the conjugate gradient algorithm that relaxed all atoms except the C_α atoms of the $\text{A}\beta_{21-30}$. Next, the C_α atoms were released and minimized again for another 20 000 steps. The system was then gradually heated in the NVT ensemble from 0 to 283 K by harmonically constraining all C_α atoms for 100 ps. Following this step, and still constraining the C_α atoms, another 200 ps were performed in the NPT ensemble at 283 K and 1 atm, followed by a brief 50 ps NPT simulation with no constraints to generate the starting configuration to be used to manufacture the pore systems. The hydrophilic pore systems were then obtained by fixing in space all water molecules that would fall outside of a sphere of radius R centered at the center of the box. All other water molecules and the $\text{A}\beta_{21-30}$ remained mobile. Production runs were then generated by performing molecular dynamic simulations on all mobile atoms. Under these conditions, all molecules interacted with each other, including mobile to nonmobile molecule interactions that included van der Waals, Coulombic, and formation of hydrogen bonds (HB) between mobile and fixed atoms. In this way, hydrophilic confinement was introduced in a natural way where the boundary that joined the fixed and mobile solvent was created without structural disruptions (Figure 1, top).

For hydrophobic pore systems, first argon atoms were placed in a periodic box of size L (following a similar protocol to the one for water above) forming a bulk system. After equilibration, the argon box was separated into two regions of fixed and mobile atoms, similar to above. Mobile argon atoms were discarded, and the equilibrated water– $\text{A}\beta_{21-30}$ system from above was used to fill the empty pore inside the fixed argon matrix with a drop of mobile water with the $\text{A}\beta_{21-30}$ at the center by exclusion of the overlapping water and argon (Figure 1, bottom). In both hydrophilic and hydrophobic pores, it was verified that the density of water at the center of the pore was close to the density of bulk water.

Due to the fact that pore radii were comparable to the size of the molecules and atoms, the irregular inner surfaces of the hydrophilic as well as of the hydrophobic pores had an intrinsic roughness (not smooth) of the same scale as the protein and water pore. Because this roughness and the hydropathy of the surface were expected to influence the dynamics of the decapeptide (e.g., ref 23), trajectories were divided into two types to separate the effects of the confined solvent from those of the surface. These two types of trajectories were (i) those in which the peptide was allowed to explore the entire volume inside the pore and (ii) those in which the center of mass of the peptide was constrained by a harmonic force to the center of the pore and thus was never allowed to be in contact with the surface. The second case was implemented using an “umbrella” pulling method, as implemented in the GROMACS package, with a spring constant of $1000 \text{ kJ mol}^{-1} \text{ nm}^{-2}$.

For convenience, the trajectories were labeled as follows. Trajectories with hydrophilic pores (fixed water) with a freely moving peptide were labeled WU (water unrestricted), trajectories with hydrophilic pores with the center of mass of the peptide constrained to the center of the pore were labeled WR (water restricted), trajectories with hydrophobic pores (fixed argon atoms) with a freely moving peptide were labeled AU (argon unrestricted), and trajectories with hydrophobic

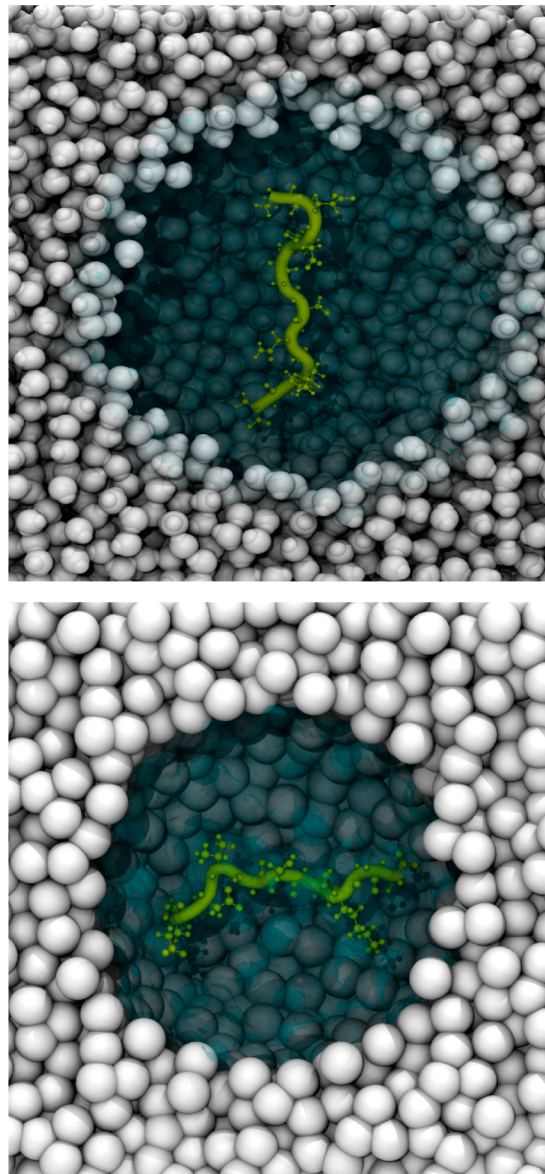


Figure 1. Interior view of pore-peptide systems at their initial conformations. Hydrophilic pores are composed of fixed water molecules (top) and hydrophobic pores of fixed argon atom (bottom). The pores shown have radius $R = 22 \text{ \AA}$ for fixed water and 20 \AA for argon. The mobile waters surrounding the decapeptide are not shown.

pores with the center of mass of the peptide constrained to the center of the pore were labeled AR (argon restricted). To generate independent trajectories using the same initial atomic positions, different trajectories were generated by assigning different velocities to each realization (according to a Maxwell–Boltzmann velocity distribution).

For each pore size, we used a total of 20 independent trajectories, with lengths 900 ns for fixed water pores (WU and WR, five trajectories each) and 500 ns for fixed argon pores (AU and AR, five trajectories each). These trajectory lengths were found to provide sufficient sampling of the available phase space by calculating the convergence of the coverage of the (Φ, Ψ) peptide backbone angles^{9,1} and verifying that at the conclusion of the simulations this coverage did not substantially increase with simulation time (Figure S1, Supporting Information) and its rate of change was close to zero (Figure

S2, Supporting Information). Total simulation time for each fixed water pore was 9 μ s while for fixed argon pores was 5 μ s, that for 7 pore sizes the accumulated simulation time was 98 μ s. For comparison, bulk trajectories amounting to 5 μ s (new trajectories) plus 4 μ s (from previous work⁸⁶) were used. Thus, bulk trajectories, all pore trajectory types, and pore sizes resulted in a total accumulated time of 107 μ s of simulation data analyzed here.

Structural Determinants. To quantify changes in the structure of the $\text{A}\beta_{21-30}$ monomer as a function of time, the radius of gyration (R_g) and specific distances between atoms were measured and labeled using the notation $R(x, y)$, where R was the distance between particular atoms in amino acid x and amino acid y , as a function of time. The distances considered in this study were the (i) $R(3, 6)$, between the two C_α atoms of Asp23 and Ser26, and (ii) $R(4, 8)$, between the two C_α atoms of Val24 and Lys28, where a small value of $R(4, 8)$ typically indicated a hydrophobic collapse between Val24 and Lys28.

The total solvent accessible surface area (SASA) of the decapeptide was calculated by adding the individual SASA from each amino acid excluding the Ala21, Ala30, Gly25, and Gly29. Secondary structure propensity per amino acid was calculated using the program STRIDE.⁹² In this study, the most commonly found structures in the decapeptide were either β -hairpins, bridges, turns, or coils (see Figure 2 for snapshots of

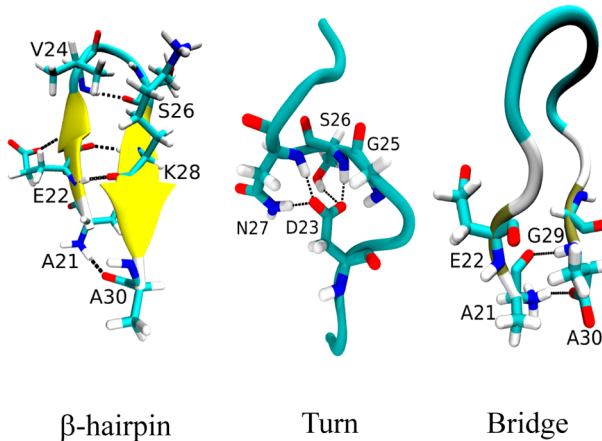


Figure 2. Example conformations from trajectory snapshots of the β_{28} hairpin, turn, and bridge structures.

these structures). The dominant β -hairpin type was the β_{28} characterized by HBs between Glu22(H)–Lys28(O), Glu22-(O)–Lys28(H), and Val24(H)–Ser26(O).⁸⁶ Bridges had at most an isolated HB between any pair of residues separated by at least one residue. Structures that were not β -hairpins nor bridges, but with distances between the C_α of Asp23/Val24 and Ser26/Lys28 of less than 7.0 Å, were classified as turns. Lastly, structures not belonging to any of the above and not a helix were classified as coil.

Hydrogen bonds (HB) were defined to exist if the distance between donor and acceptor was ≤ 3 Å and the angle θ between the donor–hydrogen–acceptor atoms was in the $160^\circ \geq \theta \leq 200^\circ$ range and calculated by using the VMD package.⁹³ Two-dimensional histograms corresponding to the negative free energy were calculated by taking R_g and SASA values as the two reaction coordinates.

RESULTS

The results of the current work are organized as follows. First, secondary structural analysis is presented for the different confinement conditions. Then, results of the radius of gyration measurements and analysis of hydrogen bonding and intramolecular distances are presented, and finally the results of correlations between SASA and R_g are presented.

Secondary Structure Analysis. A graph of the percentage of secondary structure over all trajectories as a function of decreasing pore radius (increasing confinement) is shown in Figure 3a and separately for each individual pore and trajectory

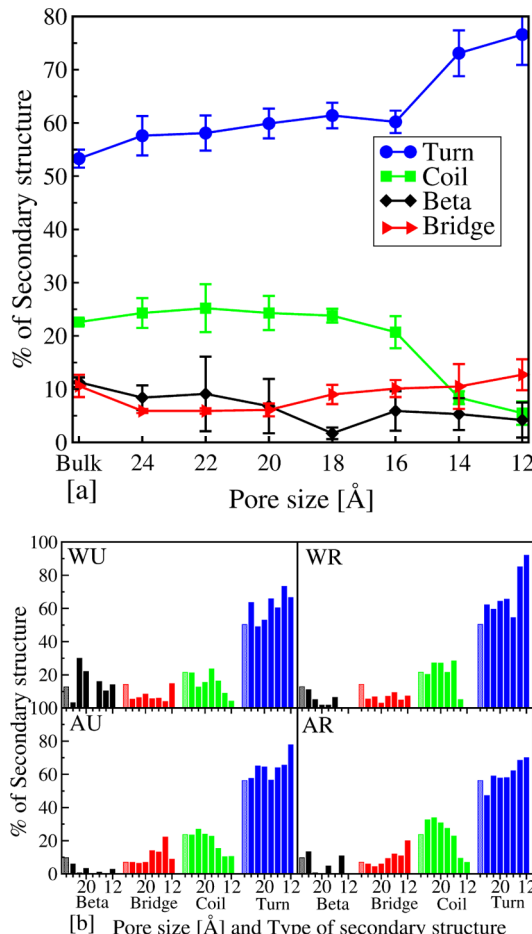


Figure 3. (a) Average secondary structure percentage as a function of decreasing pore radii obtained by considering all trajectory types (WU, WR, AU, and AR). The error bars represent the standard error of the mean. (b) Secondary structure percentages for each of the pore and trajectory types (WU, WR, AU, AR) as a function of decreasing radius of the pores. Secondary structures shown correspond to β -hairpin (black, β_{28}), bridge (red), coil (green), and turn (blue). The first bar (textured bars) in each secondary structure set corresponds to the corresponding value in a bulk system (not-confined).

type (WU, WR, AU, and AR) in Figure 3b. In these graphs only the four predominant structural forms are shown (β -hairpins, bridge, turn, and coil) for $\text{A}\beta_{21-30}$ with all others (e.g., helix) omitted due to their negligible occurrences. From Figure 3a it was evident that based on their high percentages, turns and coils dominated the structures, with the percentage of turns increasing at the expense of coil structures. In addition, the percentage of turn structures increased while that of coil structures decreased with degree of confinement for pore radii

below $R < 16 \text{ \AA}$. There was an overall reduction in the amount of β_{28} structures between bulk and the smallest pore radius (12 \AA), while no significant change was seen for the case of bridges. These trends were in general preserved when examining these percentages for each separate trajectory given in Figure 3b, although with an increased amount of fluctuations. In particular, the percentage of β_{28} structures greatly fluctuated from pore radius to pore radius, with about half of the pores not exhibiting appreciable amounts of the β_{28} structures. These fluctuations were due to the nature of the metastable β_{28} structures that, although sporadic, once formed tended to remain unbroken for tens of nanoseconds (with lifetimes on the order of 100 ns^{86}). Also, bridges were observed to be more frequent in smaller pores compared to the bulk. This was particularly true in the hydrophobic pores (AU and AR). The increase of the turn at the expense of the coil structures with increasing confinement was also preserved on a per trajectory type basis (Figure S3, Supporting Information), with an onset of this effect at a pore radius of about $R = 16 \text{ \AA}$. Detailed analysis showed that this effect was a direct consequence of the central amino acids (Val24, Gly25, and Ser26) gaining turn structure with confinement (not shown).

To assess the degree of compactness of the decapeptide as a function of confinement, we plotted in Figure 4 the average R_g

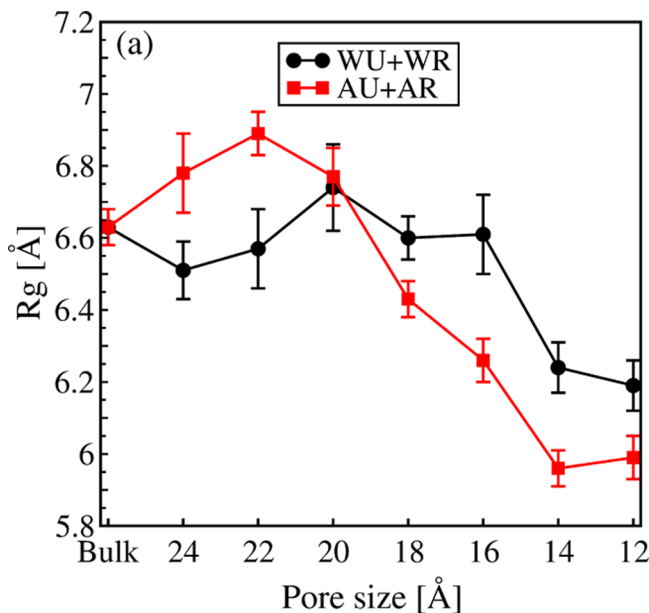


Figure 4. Dependence of R_g on decreasing pore radii for each trajectory type. The error bars represent the standard error of the mean.

per pore type (see Figure S4 for R_g separated by trajectory type, Supporting Information). This figure shows the natural structural collapse with increasing confinement starting at about $R = 18 \text{ \AA}$ for the hydrophobic pores (AU and AR) and at about $R = 14 \text{ \AA}$ for the hydrophilic pores (WU and WR). An explanation for the discrepancy of this onset, discussed in more detail below, involves the interactions between the decapeptide, water close to the pore surfaces, and surfaces of the pores. These interactions were also responsible for the lower size at higher confinement in the hydrophobic pores (more evident in the AU in Figure S4a, Supporting Information) as compared to the hydrophilic pores. At low confinement (larger pores), the differences in R_g between hydrophobic and hydrophilic pores

were due to the different content of β -hairpin in each case. A similar analysis using the end-to-end distance of the decapeptide (Figures S4b and SSa, Supporting Information) showed similar behavior, such as the onset of collapse and the consistent lower size in hydrophobic pores for $R \leq 18$ (in particular in the AU) when compared to hydrophilic pores.

Hydrogen Bonding Analysis. Average HB contacts between two amino acids were calculated by counting the total number of HBs between these two amino acids in all trajectories of the same type in a given pore and dividing by the total number of HBs occurring between all amino acid pairs. Figure 5 shows HB contact maps where each row of maps corresponds to different trajectories (WU, WR, AU, and AR) while columns correspond to bulk and three representative (24, 14, and 12 \AA) pore radii. All other contact maps for intermediate pore radii are reported in the Supporting Information (Figure S6). The most notable observation in Figure 5 was that irrespective of pore radii and trajectory type, all contact maps showed a prominent HB between Asp23 and Ser26 and that, with only few exceptions, was the most prevalent contact.

To probe the degree of influence of the HBs between Asp23 and Ser26 on structure, Figure 6 presents normalized histograms of the $R(3, 6)$ distance for all trajectory types and pore radii. In most of the cases shown in this figure, there were two peaks in the histograms for $R(3, 6) < 7.0 \text{ \AA}$ (contacts were defined for $R(3, 6) \leq 7.0 \text{ \AA}$). To analyze the nature of these peaks, we extracted the simulation frames corresponding to each of these two peaks (with $R(3, 6) \cong 5.5$ and 6.5 \AA) and analyzed their HB content (listed in Tables S1–S4, Supporting Information). From these data it was clear that the Asp23-Ser26 amino acid HB contacts found in Figure 5 were mostly composed of Asp23(O_δ)-Ser26(H_γ) and Asp23(O_δ)-Ser26(H) HBs, although the peak at $R(3, 6) \cong 5.5 \text{ \AA}$ had additional substantial contributions from other HBs (Tables S1–S4, Supporting Information). Variability of peak heights between different graphs in Figure 6 was due to slightly different HB contributions from transient secondary structure, such as β -hairpins or bridge formation (with HBs between Glu22-Lys28 or Glu22/Val24-Asn27/Gly29 or Glu22/Asp23-Lys28).

An additional observation of Figure 6 is that the AU, in contrast to the other trajectory types, had a single peak at $R(3, 6) < 7.0 \text{ \AA}$ for $12 \text{ \AA} < R \leq 18 \text{ \AA}$. As is discussed below, the omission of the second peak for these pore sizes in the AU was directly attributed to decapeptide–pore interactions missing in the other trajectory types. However, at radius $R = 12 \text{ \AA}$ all histograms showed only one peak for $R(3, 6) < 7.0 \text{ \AA}$, although at slightly different values of $R(3, 6)$ from larger pore sizes. The main source for this peak was the HB between Asp23(O_δ)-Ser26(H_γ) (Tables S1–S4, Supporting Information). This is consistent with a lack of substantial secondary structure at this pore size ($R = 12 \text{ \AA}$) since the Asp23(O_δ)-Ser26(H_γ) HB is not associated with secondary structure. The fact that the positions of these peaks were different from those of larger pore radii suggested that there may be factors other than HB playing a role in altering the $R(3, 6)$ peak position in the $R = 12 \text{ \AA}$ pores.

To examine the behavior of the dominant HBs in the context of all other HBs, we calculated all HB percentages for each trajectory at the level of the donor–acceptor atom pairs (Tables S5–S8, Supporting Information). These data reiterated the importance of the Asp23-Ser26 HBs relative to all other HBs. To better visualize and understand this observed trend, the specific values of HB percentages were graphed in Figure 7

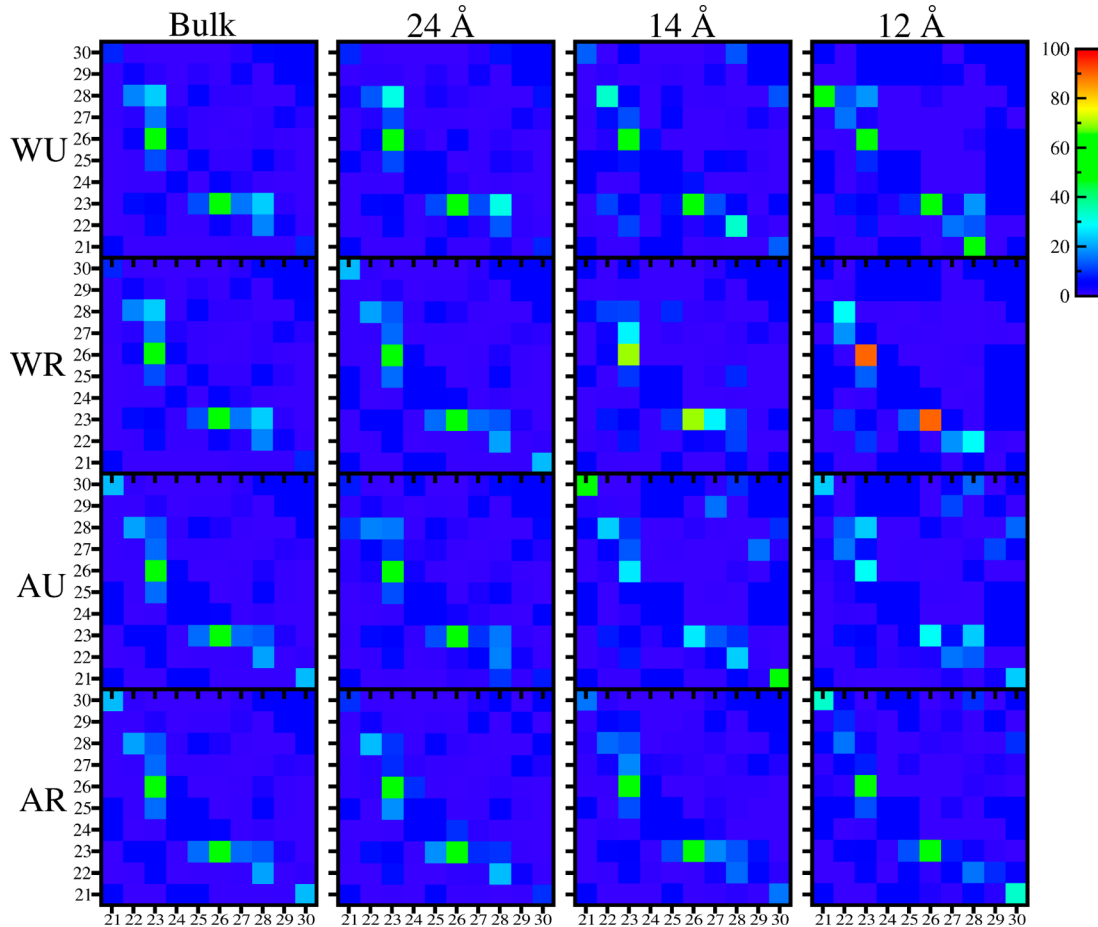


Figure 5. HB contact maps for all pore and trajectory types for the case of bulk and three representative pore radii. The legend indicates the percentage frequency of HBs from blue (low) to red (high). With few exceptions, all contact maps have a prominent HB between Asp23 and Ser26. Other important contacts are Ala21-Lys28, Glu22-Lys28, Glu22-Asn27, and Ala21-Ala30. HBs frequently were associated with structure, such as the Ala30-Ala21 and Lys28-Glu22 leading to β_2 -hairpins. However, the Ala30-Ala21 HB in AU and AR at pore radii 12 Å through 18 Å mostly corresponded to bridges, and at $R = 12$ Å, the Ala21-Lys28 in the WU did not lead to β -hairpin content, but to different structural forms.

using a specific colormap. The index number of each HB in the y -axis corresponds to a particular HB (the index number-to-HB list is presented in the last column of Tables S5–S8, in the Supporting Information). An initial observation of this figure, also supported by Figure 5, is that all colormaps exhibited a high percentage occurrence of the Asp23(O_δ)-Ser26(H) and Asp23(O_δ)-Ser26(H_γ) HBs (labels 5 and 6 in the y -axis, respectively) in most of the pores, which have been found to contribute to turn formation in bulk. However, exceptions to this observation were found in trajectory AU (and to a lesser degree in the AR) where the Ala30(O)-Ala21(H) HB (label 31 on the y -axis) was one of the strongest for pore radii equal to or smaller than 18 Å.

An interesting feature of Figure 7 was that the average HB percentage for Asp23(O_δ)-Ser26(H) and Asp23(O_δ)-Ser26(H_γ) seemed to increase with increasing confinement and reached a maximum between pore radii of 22 and 24 Å. A plot of the percentage of Asp23(O_δ)-Ser26(H_γ) as a function of confinement, however, did not show this trend as significant (with overlapping error bars—not shown). A similar plot of the Asp23(O_δ)-Ser26(H) HBs as a function of confinement (Figure 8a) showed that although the average of the data traced the increases observed in Figure 7, the initial increase in HBs was only significant for the WR trajectories. Interestingly, as a function of increasing confinement, none of the graphs in

Figure 8a showed any significant increase in this HB (in contrast with the amount of turn structure), but showed a decrease at $R = 12$ Å. The AU trajectories exhibited an additional feature, with this HB showing a significant reduction for $R \leq 18$ Å. Because this behavior was not present in the WR or AR trajectories, this trend in the HB data was attributed to interactions of the decapeptide with the hydrophobic surface. As shown below, the decapeptide in the WU trajectories was also far from the surface of the pore, thus supporting the view that the lowering of this HB was due to peptide–surface interactions. To verify that the different β -hairpin content in each trajectory was not biasing the findings on the Asp23(O_δ)-Ser26(H) HB by changing the percentages of HB in the trajectories, Figure 8b plots the percentage of Asp23(O_δ)-Ser26(H) HB content per trajectory type excluding those conformations containing β -hairpins. By comparing parts a and b of Figure 8, the following were verified, even discarding the β -hairpins: (i) the Asp23(O_δ)-Ser26(H) HB did not increase in percentage as a function of confinement, (ii) this same HB had a significant reduction at $R = 12$ Å, and (iii) the AU trajectories had a significant reduction in this HB for $R \leq 18$ Å.

By examining the end-to-end distance, it was found that with increasing level of confinement, a decreasing average end-to-end distance per pore exhibited a corresponding decrease in the combined Asp23(O_δ)-Ser26(H_γ) and Asp23(O_δ)-Ser26(H)

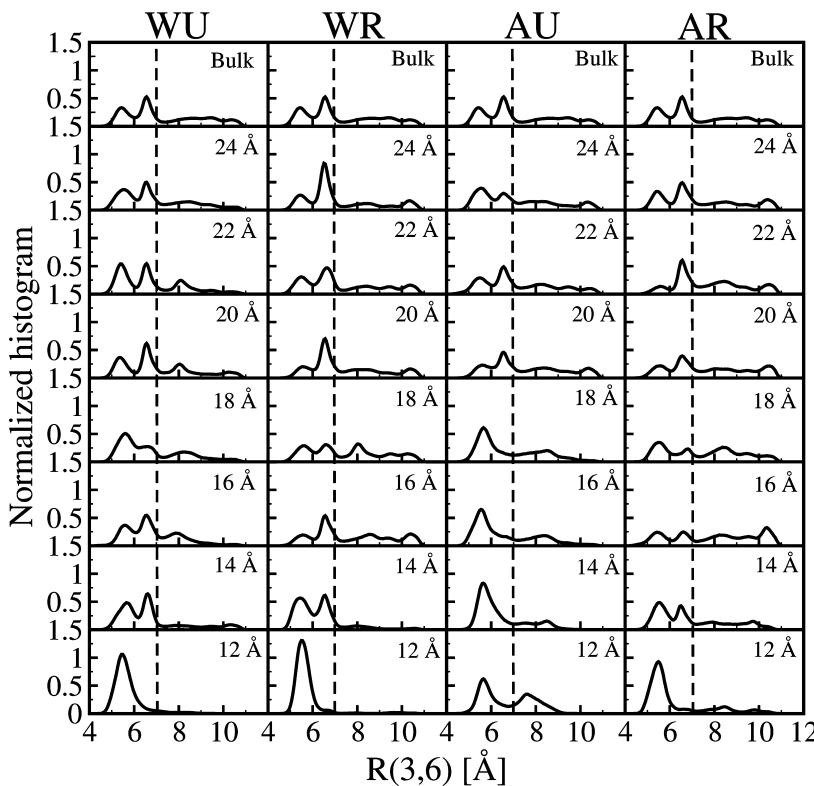


Figure 6. Normalized histograms of $R(3,6)$ for all trajectory types and pore radii. The vertical dotted line is located at 7.0 Å.

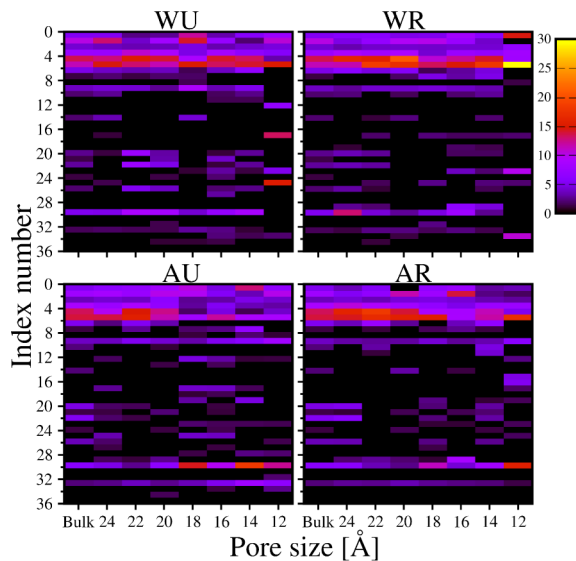


Figure 7. Individual HB donor–acceptor percentage frequency of formation vs decreasing pore radii. The HB percentages, given in the Supporting Information, are represented in color following the scale shown in the figure. The HB index number (IN) in the y-axis represents each HB (see Supporting Information, last column of Tables S5–S8, for the correspondence between IN and specific HB donor–acceptor atom pairs).

HBS (Figure S7a, Supporting Information). Thus, contrary to expectations, but similar to the R_g results above, smaller structures were not correlated to an increase in formation of the Asp23-Ser26 HBS. This suggested that the observed compactness was due to increasing confinement and not due to an increase in HB percentage. This conclusion was tested by performing a separate trajectory simulation in which a

decapeptide in bulk water was free to move except for the two C_α of Ala21 and Ala30 that were held fixed in space at a prespecified (and decreasing) end-to-end distance. Results from 1 μ s of accumulated simulation time as a function of end-to-end distances (in the 8–16 Å range) also showed a decrease in HB between Asp23 and Ser26 (Figure S7b, Supporting Information), thus showing that the compaction of the decapeptide was driven by increasing confinement and not by an increase in intrapeptide HBs, or similarly, that the structural collapse weakened the intrapeptide HB network.

When examining intrapeptide hydrophobic contacts, an analysis of the $R(4,8)$ distance (Figure S8, Supporting Information) showed that hydrophobic contacts (defined as $R(4,8) \leq 7.5$ Å) did not increase with increasing confinement. In fact, under extreme confinement ($R = 12$ Å) the average value of $R(4,8)$ for trajectories WU and WR was greater than for larger pore radii. This suggested that confinement did not increase the propensity of the decapeptide toward a hydrophobic collapse.

R_g and SASA. To assess changes in the phase space explored by the decapeptide as a function of confinement, we calculated 2D histograms (negative of the free-energy) using R_g and total SASA and show them in Figure 9 for bulk and three representative pore radii (all other histograms are available in Figure S9, Supporting Information). It was found that for pore radii with $R > 12$ Å, the region with $R_g \sim 5.5$ Å (SASA values in the range of 625–725 Å²) mostly contained β_{28} -hairpins or bridge structural forms. Structures with increased R_g and SASA usually corresponded to turns or coils. Overall, the area of the available conformational space shown in Figure 9 was greatly reduced for pore radii $R \leq 14$ Å. At extreme confinement ($R = 12$ Å) the explored phase space had a smaller range of R_g values (corresponding to the previously observed structural collapse) and seemed to occupy mostly one structural form (turn) with a

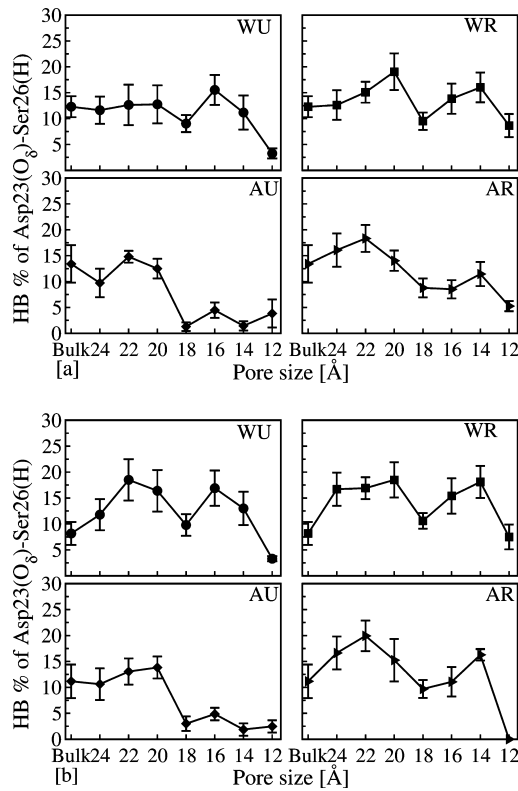


Figure 8. (a) Percentage of HBs that form between Asp23(O_{δ}) and Ser26(H) for all trajectory types as a function of pore radii. Values are taken from Figure 7. Error bars are standard error of the mean and were calculated by considering each 900 ns (WU/WR) and 500 ns (AU/AR) trajectory as a separate realization. (b) Percentage of HBs that form between Asp23(O_{δ}) and Ser26(H) for all trajectory types, but discarding all β -hairpin conformations, as a function of pore radii. For the WU, WR, and AR trajectories, this HB is mostly constant (within error) up to the highest confinement pore (the low at $R = 18 \text{ \AA}$ of WU/WR/AR is not significant) while the AU showed an uncharacteristic decrease starting at intermediate confinement.

sharp decrease of the amount of the other structures. However, at this same pore radius the areas of the plots were not the same for the hydrophilic and hydrophobic pores. The area of the parameter space was substantially smaller for the hydrophilic pores. On performing a separate trajectory with only the hydrophobic pore (AU only) but using now $R = 10 \text{ \AA}$, we obtained a phase space that resembled the size of the much reduced one in the hydrophilic pores at $R = 12 \text{ \AA}$ (shown to the right of the plots in Figure 9). The fact that by just reducing the radius of the pores in the hydrophobic case we could reproduce the bigger hydrophilic pore results suggested that the hydrophilic pores had a smaller available volume of mobile water molecules for the decapeptide. This test suggested that the reduced mobile water volume in the hydrophilic pores was due to a monolayer of relatively immobile water molecules close to the surface that effectively reduced the pore radius in the WU and WR. This monolayer can be understood by considering that water molecules in the mobile–pore interface will tend to interact (forming HBs) with the pore surface (the fixed water molecules) reducing their mobility. This situation did not happen in the hydrophobic pores as the mobile waters cannot form HBs with the pore surface (the fixed argon). Thus, these data suggested that confinement effects were more

effective (occur at larger pores) by using hydrophilic surfaces at the limit of extreme confinement.

However, although hydrophilic pores were more effective in reducing the available phase space of the decapeptide, this did not translate into smaller conformations (with smaller R_g), as can be seen from Figure 4 where hydrophilic pores in effect allowed for more extended conformations as compared to the hydrophobic. This was also supported by examining the histogram of R_g as a function of pore size, in which the WU and WR trajectories had an absence of smaller conformations in WU and WR as compared to the hydrophobic trajectories (AU and AR) at $R = 12 \text{ \AA}$ (Figure S10, Supporting Information), making the distributions narrower in the hydrophilic cases. If the restriction of phase space was directly related to a decrease in available volume, then the hydrophilic pores should have had an excess of smaller conformations. A plausible explanation for this inconsistency is that the larger conformations of the decapeptide in the hydrophilic pores (but still with $R_g < 6.5 \text{ \AA}$) were preserved over smaller conformations by forming HBs with the surface layer (monolayer) of water molecules. This explanation would require that the decapeptide stayed away from the surface of the hydrophilic pores (because of the bonding with the monolayer of water between the decapeptide and the surface of the pore) while, at the same time, not impose the same restriction in the hydrophobic pores.

To investigate this situation, we calculated the average distance between the center of mass of each amino acid and the pore surface (only using the unconstrained trajectories, WU and AU), and plotted them in Figure 10. The first observation in this figure is that the hydrophobic amino acids Val24 and Gly25 approached the surface with increasing confinement, a natural tendency of the system as it maximized the number of HBs of the mobile waters by exposing hydrophilic amino acids and burying the hydrophobic ones close to the surface. This effect, however, was more radical in the hydrophobic pores than in the hydrophilic ones. For AU at $R = 12 \text{ \AA}$, the residues Val24 through Ala30 were found to be $\sim 3 \text{ \AA}$ away from the surface while in the hydrophilic pores the amino acids in the decapeptide did not get closer than $\sim 3.5 \text{ \AA}$ to the surface. These data suggested that, on average, the decapeptide at extreme confinement was farther from the surface in the hydrophilic pores as compared to the hydrophobic ones.

One last observation of Figure 10 is that in the AU trajectories, the Val24 and Gly25 were observed to be closer to the pore surface for $R \leq 18 \text{ \AA}$ as compared to the WU trajectories. Because this closeness at this range of pore sizes coincided with the onset in the AU of a single peak in the $R(3, 6)$ histograms (Figure 6), the decrease in the Asp23(O_{δ})-Ser26(H) HBs (Figure 8), and the decrease in R_g and end-to-end (Figures 4, S4, and S5, Supporting Information), these data suggested that the close proximity of the decapeptide to the hydrophobic surface allowed for decapeptide–pore interactions responsible for these structural changes.

DISCUSSION AND CONCLUSIONS

In this study, all-atom molecular-dynamics simulations were presented investigating the dynamics of an IDP, the folding nucleus of the amyloid β -peptide, the $A\beta_{21-30}$, under hydrophilic and hydrophobic confinement. The main goal was to examine the behavior of this IDP under confinement and whether intramolecular interactions and structure were differentially affected by the nature of the surface of the confining pore and the confined water. An interesting perspective of using

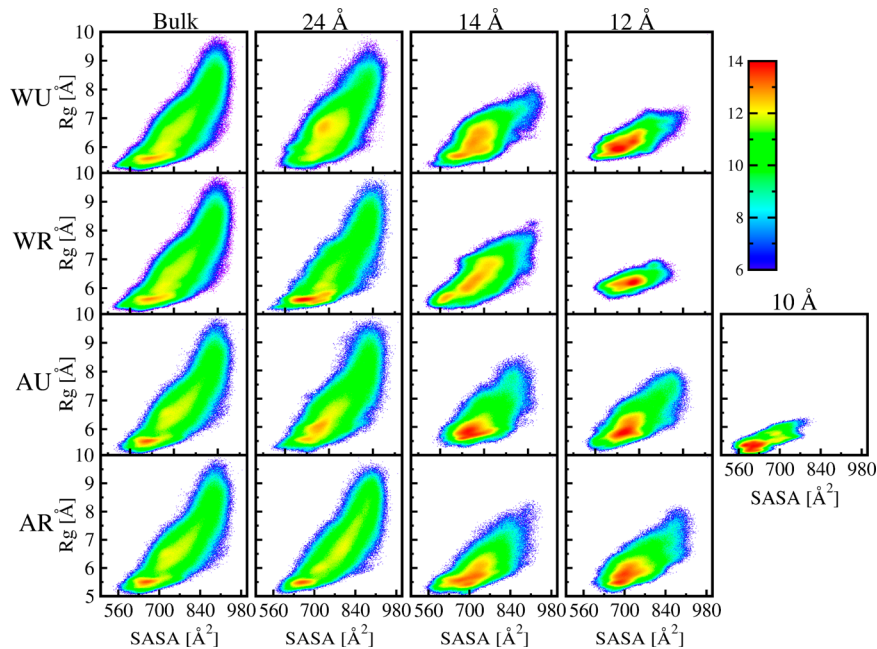


Figure 9. Histogram of the number of conformations with a given R_g and SASA value pair for the different pore and trajectory types (negative of the free energy). Trajectory AU shows an additional map corresponding to a pore of radius of 10 Å.

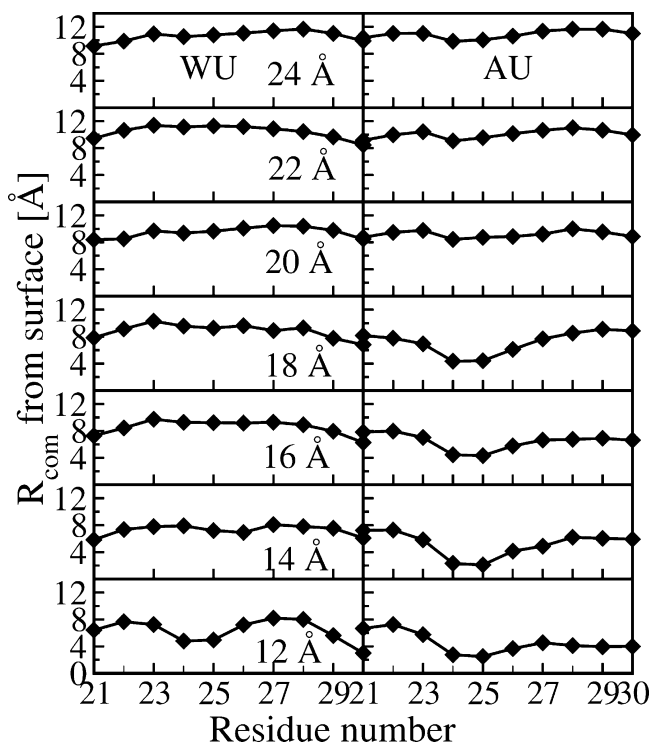


Figure 10. Average distance between the center of mass (com) of each amino acid and the pore surface for the WU and AU trajectory types. Each graph corresponds to a different pore radius. In the plots, a small value of R_{com} corresponds to close proximity to the surface of the pore.

an IDP over a protein with a native structure was that intrapeptide HBs and their relationship to structure could be thoroughly analyzed at all pore sizes without the protein collapsing to its native folding state. An additional goal was to investigate whether metastable β -hairpins would form at different rates and percentages as those observed in a previous study.⁸⁶

This work stands apart from other studies^{2,5,7,9–13,17,21,23,24,32,41,42,46,94–96} not only in using an IDP as the testing protein but also in the structure of the confining pores. The pores were constructed by immobilizing water molecules or argon atoms with positions drawn from their respective normal liquid state. Because of their hydrophobicity, these surfaces may be useful to understand complex biological systems, for example, those found inside the *Escherichia coli* chaperonin GroEL, a molecular chaperone that assists proteins to fold in vivo.⁹⁷ Previous computational studies have modeled the interior of molecular chaperones by using smooth hydrophobic and hydrophilic surfaces.²³ By construction, here the boundaries created by the pore walls were not smooth, but rough due to the random atomic positions of the immobilized atoms. This characteristic roughness of the pores, in addition to being a closer representation of the surface roughness found in macromolecules, is of importance as rough and smooth surfaces have been shown to lead to contrasting behavior in other systems.^{49–52}

To achieve the goal of separately assessing changes in the dynamics of the $A\beta_{21–30}$ decapeptide due to the pore surface and the confined water, trajectories with a decapeptide restricted to the center of the pore (WR and AR) were performed in tandem with those of unrestricted decapeptides (WU and AU). Results showed that in general there were no substantial differences in the quantities analyzed in these two different system realizations, with some notable exceptions in the AU. Specifically, the WR and WU trajectories were very similar to each other, suggesting that hydrophilic interfaces may play a smaller role than the confined solvent. However, comparing the histogram of $R(3, 6)$ distances between the WR/WU/AR and the AU trajectories revealed that of the two peaks at $R(3, 6) \cong 5.5$ and 6.5 Å appearing in the first group, the one at $R(3, 6) = 6.5$ Å was missing in the AU for pores with $R \leq 18$ Å. This missing peak was reflected in a more compact structure in the AU, as seen in its lower R_g and end-to-end values at high confinement. Also, the Asp23(O_δ)-Ser26(H) HB between the

WR, WU, and AR was in essence unchanged until high confinement while those for the AU decayed already at intermediate confinement, suggesting that hydrophobic surfaces (through peptide–surface interactions) may affect intrapeptide HBs more than the confined solvent. The similarities between the WR and AR, and differences between the AR and AU, suggested that while the decapeptide was restricted to the center of the pore it did not feel the effects of the surface (only effects from the confined solvent), while in the AU it did feel the surface by virtue of the attractive hydrophobic interactions between the decapeptide and the argon surface. Because it is only at $R = 12 \text{ \AA}$ that the AR and AU exhibited similar behavior, this finding suggested that the confined water, acting through the monolayer of water molecules close to the surface (strong water–pore HB bonding in the hydrophilic and no HB bonding in the hydrophobic), had a short-ranged influence on the interior of the pore and on the dynamics of the decapeptide, consistent with the similarities found in the WR, WU, and AR trajectories for $R \geq 14 \text{ \AA}$.

For the case of the freely moving unrestricted $\text{A}\beta_{21-30}$ (AU and WU), results presented here suggested that for the case of the hydrophilic confinement, the “stiff” (less mobile) monolayer of water kept the decapeptide away from the surface. A similar layer of water was also observed in a study by Faeder et. al, in which the authors also noticed that the water molecules inside reverse micelles formed an immobile layer bound to the surface of the reverse micelles.⁹⁸ Although structural analysis of the distribution of water molecules in the hydrophobic pores presented above confirmed the presence of a structured monolayer of water close to its surface (data not shown), the effects of this monolayer on the structure and dynamics of the decapeptide were small compared to the hydrophilic confinement. By comparison, the hydrophobic pores behaved more like a “well-oiled” water–argon interface that did not keep the decapeptide away from the surface. Indeed, the distances of the hydrophobic amino acids to the surface (namely Val and Gly) were smaller than in the hydrophilic pores. These properties of the monolayers of waters for each pore type had consequences on the available volume to the decapeptide, resulting in a narrow distribution of R_g and a severe restriction in the exploration of the conformational phase space in the WU (and WR) at extreme confinement ($R = 12 \text{ \AA}$). It is interesting that the average value of R_g in the hydrophobic AU case was smaller than the other trajectories for $R \leq 18 \text{ \AA}$. Although the quantities analyzed here did not clearly reveal a single reason for this behavior, and in most cases would support the opposite behavior (larger phase space, larger mobile water volume), it is likely that this was also due to decapeptide–pore interactions.

In the case of extreme confinement ($R = 12 \text{ \AA}$), our results in the hydrophobic pores indicated that the $\text{A}\beta_{21-30}$ preferred to stay close to the confining wall without forming any secondary structure. This result is in agreement with recent work in which the Trp cage protein in nonpolar confinement was preferentially found close to the confined wall in a collapsed coil configuration.²³ Similar results were noticed in another study by Jamadagni et al. at alkane–water interface.⁵⁶ However, in the current work, this closeness between the decapeptide and the confining wall or water–argon interface was noticed only in smaller pores ($R \leq 18 \text{ \AA}$). For larger pores ($R > 18 \text{ \AA}$), we did not notice this effect in the position of the decapeptide in either type of pore. Because in all of the other quantities examined here there was also no significant change relative to the bulk for

$R > 18 \text{ \AA}$, this suggests that the effects of confinement and the confined solvent are short-ranged (they depend on the relative size of the peptide to the pore size). One reason for this could be a combination of a long time scale for the decapeptide to find the surface in the larger pores and a low number of hydrophobic residues in the decapeptide.

Earlier studies^{8-10,18,26,29,45,95} on confinement showed that the folding rate of proteins was increased at medium-sized pores by decreasing (or destabilizing the unfolded states) the reaction barrier to reach the folded state. In the case studied here, the $\text{A}\beta_{21-30}$ an IDP, there is no folded state. However, the main structures in the $\text{A}\beta_{21-30}$ have been widely characterized as turns.^{72,80,81,86} The results presented above indicated that confinement similarly increased the percentage amount of turns, while decreasing the coil and keeping β -hairpin amounts intact, for smaller pores in all trajectory types. On the other hand, the HB percentage between Asp23-Ser26, which has been correlated to the formation of turns in bulk simulations, did not show a corresponding increase, and even decreased with degree of confinement, meaning that the increased turn structures were more compact but also not dependent on intramolecular HBs. Interestingly, hydrophobic interactions (between Val24 and Lys28) did not seem to have played a significant role at any level of confinement.

Besides the general question of structure and dynamics under confinement, these results also have relevance to the broader question of aggregation and assembly in Alzheimer’s disease. In AD there is evidence that indicates the existence of turns or loops in the $\text{A}\beta_{21-30}$ amino acid region of the full-length $\text{A}\beta$ when forming part of prefibrillar intermediates or fibrils specifically of $\text{A}\beta40$,^{99,100} $\text{A}\beta42$, and $\text{A}\beta_{10-35}$.¹⁰¹ Because of confined and crowded environments in vivo, an enhanced turn structure in this 21–30 region may play an important role on the kinetics and pathways of oligomer and fibril formation.

ASSOCIATED CONTENT

S Supporting Information

Detailed simulation results. This material is available free of charge via the Internet at <http://pubs.acs.org>.

AUTHOR INFORMATION

Corresponding Author

*E-mail: ccruz@drexel.edu. Tel.: (215) 895-2739. Fax: (215) 895-5934.

Notes

The authors declare no competing financial interest.

ACKNOWLEDGMENTS

Computational time was provided in part by XSEDE computational resources grant TG-MCB110142.

ABBREVIATIONS

$\text{A}\beta$, amyloid β -protein; IDP, intrinsically disordered peptide; AD, Alzheimer’s disease; HB, hydrogen bond; MD, molecular dynamics; SASA, solvent accessible surface area; SB, salt bridge

REFERENCES

- (1) Zhou, H. X.; Rivas, G. N.; Minton, A. P. Macromolecular Crowding and Confinement: Biochemical, Biophysical, and Potential Physiological Consequences. *Annu. Rev. Biophys.* **2008**, *37*, 375–397.
- (2) Eggers, D. K.; Valentine, J. S. Molecular Confinement Influences Protein Structure and Enhances Thermal Protein Stability. *Protein Sci.* **2001**, *10* (2), 250–261.

- (3) Jarvet, J.; Danielsson, J.; Damberg, P.; Oleszczuk, M.; Graeslund, A. Positioning of the Alzheimer α -Beta(1–40) Peptide in SDS Micelles Using NMR and Paramagnetic Probes. *J. Biomol. NMR* **2007**, *39* (1), 63–72.
- (4) Kumar, C. V.; Chaudhari, A. Proteins Immobilized at the Galleries of Layered Alpha-Zirconium Phosphate: Structure and Activity Studies. *J. Am. Chem. Soc.* **2000**, *122* (5), 830–837.
- (5) Peterson, R. W.; Anbalagan, K.; Tommos, C.; Wand, A. J. Forced Folding and Structural Analysis of Metastable Proteins. *J. Am. Chem. Soc.* **2004**, *126* (31), 9498–9499.
- (6) Wei, Y.; Xu, J. G.; Feng, Q. W.; Dong, H.; Lin, M. D. Encapsulation of Enzymes in Mesoporous Host Materials Via the Nonsurfactant-Templated Sol–Gel Process. *Mater. Lett.* **2000**, *44* (1), 6–11.
- (7) Baumketner, A.; Jewett, A.; Shea, J. E. Effects of Confinement in Chaperonin Assisted Protein Folding: Rate Enhancement by Decreasing the Roughness of the Folding Energy Landscape. *J. Mol. Biol.* **2003**, *332* (3), 701–713.
- (8) Bhattacharya, A.; Best, R. B.; Mittal, J. Smoothing of the Gb1 Hairpin Folding Landscape by Interfacial Confinement. *Biophys. J.* **2012**, *103* (3), 596–600.
- (9) Cheung, M. S.; Klimov, D.; Thirumalai, D. Molecular Crowding Enhances Native State Stability and Refolding Rates of Globular Proteins. *Proc. Natl. Acad. Sci. U.S.A.* **2005**, *102* (13), 4753–4758.
- (10) Cheung, M. S.; Thirumalai, D. Effects of Crowding and Confinement on the Structures of the Transition State Ensemble in Proteins. *J. Phys. Chem. B* **2007**, *111* (28), 8250–8257.
- (11) England, J.; Lucent, D.; Pande, V. Rattling the Cage: Computational Models of Chaperonin-Mediated Protein Folding. *Curr. Opin. Struct. Biol.* **2008**, *18* (2), 163–169.
- (12) England, J. L.; Lucent, D.; Pande, V. S. A Role for Confined Water in Chaperonin Function. *J. Am. Chem. Soc.* **2008**, *130* (36), 11838–11839.
- (13) Friedel, M.; Sheeler, D. J.; Shea, J. E. Effects of Confinement and Crowding on the Thermodynamics and Kinetics of Folding of a Minimalist Beta-Barrel Protein. *J. Chem. Phys.* **2003**, *118* (17), 8106–8113.
- (14) Garcia, A. E.; Onuchic, J. N. Folding a Protein in a Computer: An Atomic Description of the Folding/Unfolding of Protein A. *Proc. Natl. Acad. Sci. U.S.A.* **2003**, *100* (24), 13898–13903.
- (15) Hatters, D. M.; Minton, A. P.; Howlett, G. J. Macromolecular Crowding Accelerates Amyloid Formation by Human Apolipoprotein C-II. *J. Biol. Chem.* **2002**, *277* (10), 7824–7830.
- (16) Hayer-Hartl, M.; Minton, A. P. A Simple Semiempirical Model for the Effect of Molecular Confinement Upon the Rate of Protein Folding. *Biochemistry* **2006**, *45* (44), 13356–13360.
- (17) Jewett, A. I.; Baumketner, A.; Shea, J. E. Accelerated Folding in the Weak Hydrophobic Environment of a Chaperonin Cavity: Creation of an Alternate Fast Folding Pathway. *Proc. Natl. Acad. Sci. U.S.A.* **2004**, *101* (36), 13192–13197.
- (18) Klimov, D. K.; Newfield, D.; Thirumalai, D. Simulations of Beta-Hairpin Folding Confined to Spherical Pores Using Distributed Computing. *Proc. Natl. Acad. Sci. U.S.A.* **2002**, *99* (12), 8019–8024.
- (19) Lucent, D.; England, J.; Pande, V. Inside the Chaperonin Toolbox: Theoretical and Computational Models for Chaperonin Mechanism. *Phys. Biol.* **2009**, *6* (1), 015003–015010.
- (20) O'Brien, E. P.; Stan, G.; Thirumalai, D.; Brooks, B. R. Factors Governing Helix Formation in Peptides Confined to Carbon Nanotubes. *Nano Lett.* **2008**, *8* (11), 3702–3708.
- (21) Rathore, N.; Knotts, T. A.; de Pablo, J. J. Confinement Effects on the Thermodynamics of Protein Folding: Monte Carlo Simulations. *Biophys. J.* **2006**, *90* (5), 1767–1773.
- (22) Sorin, E. J.; Pande, V. S. Nanotube Confinement Denatures Protein Helices. *J. Am. Chem. Soc.* **2006**, *128* (19), 6316–6317.
- (23) Tian, J. H.; Garcia, A. E. Simulation Studies of Protein Folding/Unfolding Equilibrium under Polar and Nonpolar Confinement. *J. Am. Chem. Soc.* **2011**, *133* (38), 15157–15164.
- (24) Tian, J. H.; Garcia, A. E. Simulations of the Confinement of Ubiquitin in Self-Assembled Reverse Micelles. *J. Chem. Phys.* **2011**, *134* (22), 225101–225111.
- (25) Ziv, G.; Haran, G.; Thirumalai, D. Ribosome Exit Tunnel Can Entropically Stabilize Alpha-Helices. *Proc. Natl. Acad. Sci. U.S.A.* **2005**, *102* (52), 18956–18961.
- (26) Kim, Y. C.; Best, R. B.; Mittal, J. Macromolecular Crowding Effects on Protein–Protein Binding Affinity and Specificity. *J. Chem. Phys.* **2010**, *133* (20), 205101–205107.
- (27) Mittal, J.; Best, R. B. Dependence of Protein Folding Stability and Dynamics on the Density and Composition of Macromolecular Crowders. *Biophys. J.* **2010**, *98* (2), 315–320.
- (28) Mittal, J.; Hummer, G. Interfacial Thermodynamics of Confined Water near Molecularly Rough Surfaces. *Faraday Discuss.* **2010**, *146*, 341–352.
- (29) Rosen, J.; Kim, Y. C.; Mittal, J. Modest Protein-Crowder Attractive Interactions Can Counteract Enhancement of Protein Association by Intermolecular Excluded Volume Interactions. *J. Phys. Chem. B* **2011**, *115* (11), 2683–2689.
- (30) Rosen, J.; Kim, Y. C.; Mittal, J. Macromolecular Crowding Effects on Multiprotein Binding Equilibria: Molecular Simulation and Theory. *Biophys. J.* **2011**, *100* (3), 614–614.
- (31) Takagi, F.; Koga, N.; Takada, S. How Protein Thermodynamics and Folding Mechanisms Are Altered by the Chaperonin Cage: Molecular Simulations. *Proc. Natl. Acad. Sci. U.S.A.* **2003**, *100* (20), 11367–11372.
- (32) Minton, A. P. Confinement as a Determinant of Macromolecular Structure and Reactivity. *Biophys. J.* **1992**, *63* (4), 1090–1100.
- (33) Zimmerman, S. B.; Minton, A. P. Macromolecular Crowding—Biochemical, Biophysical, and Physiological Consequences. *Annu. Rev. Biophys. Biomol. Struct.* **1993**, *22*, 27–65.
- (34) Minton, A. P. Effects of Macromolecular Crowding on Molecular Recognition. *Biophys. J.* **1994**, *66* (2), A68–A68.
- (35) Minton, A. P. Macromolecular Crowding—A Foreword. *Biophys. Chem.* **1995**, *57* (1), 1–2.
- (36) Minton, A. P. Implications of Macromolecular Crowding for Protein Assembly. *Curr. Opin. Struct. Biol.* **2000**, *10* (1), 34–39.
- (37) Minton, A. P. The Influence of Macromolecular Crowding and Macromolecular Confinement on Biochemical Reactions in Physiological Media. *J. Biol. Chem.* **2001**, *276* (14), 10577–10580.
- (38) Minton, A. P.; Colclasure, G. C.; Parker, J. C. Model for the Role of Macromolecular Crowding in Regulation of Cellular-Volume. *Proc. Natl. Acad. Sci. U.S.A.* **1992**, *89* (21), 10504–10506.
- (39) Minton, A. P.; Wilf, J. Effect of Macromolecular Crowding Upon the Structure and Function of an Enzyme—Glyceraldehyde-3-Phosphate Dehydrogenase. *Biochemistry* **1981**, *20* (17), 4821–4826.
- (40) Zhou, H. X. Polymer Models of Protein Stability, Folding, and Interactions. *Biochemistry* **2004**, *43* (8), 2141–2154.
- (41) Zhou, H. X. Helix Formation inside a Nanotube: Possible Influence of Backbone-Water Hydrogen Bonding by the Confining Surface through Modulation of Water Activity. *J. Chem. Phys.* **2007**, *127* (24), 245101–245104.
- (42) Zhou, H. X. Protein Folding in Confined and Crowded Environments. *Arch. Biochem. Biophys.* **2008**, *469* (1), 76–82.
- (43) Zhou, H. X.; Dill, K. A. Stabilization of Proteins in Confined Spaces. *Biochemistry* **2001**, *40* (38), 11289–11293.
- (44) Tang, Y. C.; Chang, H. C.; Roeben, A.; Wischnewski, D.; Wischnewski, N.; Kerner, M. J.; Hartl, F. U.; Hayer-Hartl, M. Structural Features of the GroEL-GroES Nano-Cage Required for Rapid Folding of Encapsulated Protein. *Cell* **2006**, *125* (5), 903–914.
- (45) Thirumalai, D.; Klimov, D. K.; Lorimer, G. H. Caging Helps Proteins Fold. *Proc. Natl. Acad. Sci. U.S.A.* **2003**, *100* (20), 11195–11197.
- (46) Lucent, D.; Vishal, V.; Pande, V. S. Protein Folding under Confinement: A Role for Solvent. *Proc. Natl. Acad. Sci. U.S.A.* **2007**, *104* (25), 10430–10434.

- (47) Lucent, D.; Snow, C. D.; Aitken, C. E.; Pande, V. S. Non-Bulk-Like Solvent Behavior in the Ribosome Exit Tunnel. *PLoS Comput. Biol.* **2010**, *6* (10), 1000963–1000968.
- (48) Zuo, G. H.; Hu, J.; Fang, H. P. Effect of the Ordered Water on Protein Folding: An Off-Lattice Gō-Like Model Study. *Phys. Rev. E* **2009**, *79* (3), 031925–031930.
- (49) Hummer, G.; Rasaiah, J. C.; Noworyta, J. P. Water Conduction through the Hydrophobic Channel of a Carbon Nanotube. *Nature* **2001**, *414* (6860), 188–190.
- (50) Yin, H.; Feng, G. G.; Clore, G. M.; Hummer, G.; Rasaiah, J. C. Water in the Polar and Nonpolar Cavities of the Protein Interleukin-1 Beta. *J. Phys. Chem. B* **2010**, *114* (49), 16290–16297.
- (51) Yin, H.; Hummer, G.; Rasaiah, J. C. Metastable Water Clusters in the Nonpolar Cavities of the Thermostable Protein Tetrabrachion. *J. Am. Chem. Soc.* **2007**, *129* (23), 7369–7377.
- (52) Lane, J. M. D.; Chandross, M.; Stevens, M. J.; Grest, G. S. Water in Nanoconfinement between Hydrophilic Self-Assembled Monolayers. *Langmuir* **2008**, *24* (10), 5209–5212.
- (53) Meng, L. Y.; Li, Q. K.; Shuai, Z. G. Effects of Size Constraint on Water Filling Process in Nanotube. *J. Chem. Phys.* **2008**, *128* (13), 134703–134710.
- (54) Won, C. Y.; Joseph, S.; Aluru, N. R. Effect of Quantum Partial Charges on the Structure and Dynamics of Water in Single-Walled Carbon Nanotubes. *J. Chem. Phys.* **2006**, *125* (11), 114701–114709.
- (55) Athawale, M. V.; Jamadagni, S. N.; Garde, S. How Hydrophobic Hydration Responds to Solute Size and Attractions: Theory and Simulations. *J. Chem. Phys.* **2009**, *131* (11), 115102–115110.
- (56) Jamadagni, S. N.; Godawat, R.; Dordick, J. S.; Garde, S. How Interfaces Affect Hydrophobically Driven Polymer Folding. *J. Phys. Chem. B* **2009**, *113* (13), 4093–4101.
- (57) Jamadagni, S. N.; Godawat, R.; Garde, S. How Surface Wettability Affects the Binding, Folding, and Dynamics of Hydrophobic Polymers at Interfaces. *Langmuir* **2009**, *25* (22), 13092–13099.
- (58) Lorenz, C. D.; Lane, J. M. D.; Chandross, M.; Stevens, M. J.; Grest, G. S. Molecular Dynamics Simulations of Water Confined between Matched Pairs of Hydrophobic and Hydrophilic Self-Assembled Monolayers. *Langmuir* **2009**, *25* (8), 4535–4542.
- (59) Sansom, M. S. P.; Kerr, I. D.; Breed, J.; Sankararamakrishnan, R. Water in Channel-Like Cavities: Structure and Dynamics. *Biophys. J.* **1996**, *70* (2), 693–702.
- (60) Garner, E.; Guilliot, S.; Dunker, A. K.; Romero, P.; Obradovic, Z. Predicting Long Disordered Regions in Protein from Amino Acid Sequence. *Biophys. J.* **1998**, *74* (2), A281–A281.
- (61) Obradovic, Z.; Peng, K.; Vucetic, S.; Radivojac, P.; Brown, C. J.; Dunker, A. K. Predicting Intrinsic Disorder from Amino Acid Sequence. *Proteins* **2003**, *53* (6), 566–572.
- (62) Dyson, H. J.; Wright, P. E. Insights into the Structure and Dynamics of Unfolded Proteins from Nuclear Magnetic Resonance. *Unfolded Proteins* **2002**, *62*, 311–340.
- (63) Tompa, P. The Interplay between Structure and Function in Intrinsically Unstructured Proteins. *FEBS Lett.* **2005**, *579* (15), 3346–3354.
- (64) Uversky, V. N. Natively Unfolded Proteins: A Point Where Biology Waits for Physics. *Protein Sci.* **2002**, *11* (4), 739–756.
- (65) Uversky, V. N. Amyloidogenesis of Natively Unfolded Proteins. *Curr. Alzheimer Res.* **2008**, *5* (3), 260–287.
- (66) Wright, P. E.; Dyson, H. J. Intrinsically Unstructured Proteins: Re-Assessing the Protein Structure-Function Paradigm. *J. Mol. Biol.* **1999**, *293* (2), 321–331.
- (67) Yang, M. F.; Teplow, D. B. Amyloid Beta-Protein Monomer Folding: Free-Energy Surfaces Reveal Alloform-Specific Differences. *J. Mol. Biol.* **2008**, *384* (2), 450–464.
- (68) Urbanc, B.; Cruz, L.; Teplow, D. B.; Stanley, H. E. Computer Simulations of Alzheimer's Amyloid Beta-Protein Folding and Assembly. *Curr. Alzheimer Res.* **2006**, *3* (5), 493–504.
- (69) Baumketner, A.; Bernstein, S. L.; Wyttenbach, T.; Bitan, G.; Teplow, D. B.; Bowers, M. T.; Shea, J. E. Amyloid Beta-Protein Monomer Structure: A Computational and Experimental Study. *Protein Sci.* **2006**, *15* (3), 420–428.
- (70) Bernstein, S. L.; Wyttenbach, T.; Baumketner, A.; Shea, J. E.; Bitan, G.; Teplow, D. B.; Bowers, M. T. Amyloid Beta-Protein: Monomer Structure and Early Aggregation States of a Beta 42 and Its Pro(19) Alloform. *J. Am. Chem. Soc.* **2005**, *127* (7), 2075–2084.
- (71) Urbanc, B.; Cruz, L.; Yun, S.; Buldyrev, S. V.; Bitan, G.; Teplow, D. B.; Stanley, H. E. In Silico Study of Amyloid Beta-Protein Folding and Oligomerization. *Proc. Natl. Acad. Sci. U.S.A.* **2004**, *101* (50), 17345–17350.
- (72) Lazo, N. D.; Grant, M. A.; Condron, M. C.; Rigby, A. C.; Teplow, D. B. On the Nucleation of Amyloid Beta-Protein Monomer Folding. *Protein Sci.* **2005**, *14* (6), 1581–1596.
- (73) Lee, J. P.; Stimson, E. R.; Ghilardi, J. R.; Mantyh, P. W.; Lu, Y. A.; Felix, A. M.; Llanos, W.; Behbin, A.; Cummings, M.; Van Crieging, M.; et al. 1H NMR of Beta Amyloid Peptide Congeners in Water Solution. Conformational Changes Correlate with Plaque Competence. *Biochemistry* **1995**, *34* (15), 5191–5200.
- (74) Zhang, S.; Iwata, K.; Lachenmann, M. J.; Peng, J. W.; Li, S.; Stimson, E. R.; Lu, Y.; Felix, A. M.; Maggio, J. E.; Lee, J. P. The Alzheimer's Peptide a Beta Adopts a Collapsed Coil Structure in Water. *J. Struct. Biol.* **2000**, *130* (2–3), 130–141.
- (75) Balbach, J. J.; Ishii, Y.; Antzutkin, O. N.; Leapman, R. D.; Rizzo, N. W.; Dyda, F.; Reed, J.; Tycko, R. Amyloid Fibril Formation by a Beta 16–22, a Seven-Residue Fragment of the Alzheimer's Beta-Amyloid Peptide, and Structural Characterization by Solid State NMR. *Biochemistry* **2000**, *39* (45), 13748–13759.
- (76) Ma, B.; Nussinov, R. Stabilities and Conformations of Alzheimer's Beta -Amyloid Peptide Oligomers (Abeta 16–22, Abeta 16–35, and Abeta 10–35): Sequence Effects. *Proc. Natl. Acad. Sci. U.S.A.* **2002**, *99* (22), 14126–14131.
- (77) Serpell, L. C. Alzheimer's Amyloid Fibrils: Structure and Assembly. *Biochim. Biophys. Acta* **2000**, *1502* (1), 16–30.
- (78) Wei, G.; Shea, J. E. Effects of Solvent on the Structure of the Alzheimer Amyloid-Beta(25–35) Peptide. *Biophys. J.* **2006**, *91* (5), 1638–1647.
- (79) Zanuy, D.; Ma, B.; Nussinov, R. Short Peptide Amyloid Organization: Stabilities and Conformations of the Islet Amyloid Peptide Nfgail. *Biophys. J.* **2003**, *84* (3), 1884–1894.
- (80) Cruz, L.; Urbanc, B.; Borreguero, J. M.; Lazo, N. D.; Teplow, D. B.; Stanley, H. E. Solvent and Mutation Effects on the Nucleation of Amyloid Beta-Protein Folding. *Proc. Natl. Acad. Sci. U.S.A.* **2005**, *102* (51), 18258–18263.
- (81) Baumketner, A.; Bernstein, S. L.; Wyttenbach, T.; Lazo, N. D.; Teplow, D. B.; Bowers, M. T.; Shea, J. E. Structure of the 21–30 Fragment of Amyloid Beta-Protein. *Protein Sci.* **2006**, *15* (6), 1239–1247.
- (82) Jorgensen, W. L.; Madura, J. D. Temperature and Size Dependence for Monte-Carlo Simulations of TIP4P Water. *Mol. Phys.* **1985**, *56* (6), 1381–1392.
- (83) Kaminski, G. A.; Friesner, R. A.; Tirado-Rives, J.; Jorgensen, W. L. Evaluation and Reparametrization of the OPLS-AA Force Field for Proteins Via Comparison with Accurate Quantum Chemical Calculations on Peptides. *J. Phys. Chem. B* **2001**, *105* (28), 6474–6487.
- (84) Lindahl, E.; Hess, B.; van der Spoel, D. GROMACS 3.0: A Package for Molecular Simulation and Trajectory Analysis. *J. Mol. Model.* **2001**, *7* (8), 306–317.
- (85) Berendsen, H. J. C.; Vandervelpen, D.; Vandrunen, R. GROMACS—A Message-Passing Parallel Molecular-Dynamics Implementation. *Comput. Phys. Commun.* **1995**, *91* (1–3), 43–56.
- (86) Cruz, L.; Rao, J. S.; Teplow, D. B.; Urbanc, B. Dynamics of Metastable Beta-Hairpin Structures in the Folding Nucleus of Amyloid Beta-Protein. *J. Phys. Chem. B* **2012**, *116* (22), 6311–6325.
- (87) Berendsen, H. J. C.; Postma, J. P. M.; Vangunsteren, W. F.; Dinola, A.; Haak, J. R. Molecular-Dynamics with Coupling to an External Bath. *J. Chem. Phys.* **1984**, *81* (8), 3684–3690.
- (88) Miyamoto, S.; Kollman, P. A. SETTLE—An Analytical Version of the Shake and Rattle Algorithm for Rigid Water Models. *J. Comput. Chem.* **1992**, *13* (8), 952–962.

- (89) Hess, B.; Bekker, H.; Berendsen, H. J. C.; Fraaije, J. G. E. M. LINCS: A Linear Constraint Solver for Molecular Simulations. *J. Comput. Chem.* **1997**, *18* (12), 1463–1472.
- (90) Essmann, U.; Perera, L.; Berkowitz, M. L.; Darden, T.; Lee, H.; Pedersen, L. G.; Smooth, A. Particle Mesh Ewald Method. *J. Chem. Phys.* **1995**, *103* (19), 8577–8593.
- (91) Scott, K. A.; Alonso, D. O. V.; Sato, S.; Fersht, A. R.; Daggett, V. Conformational Entropy of Alanine Versus Glycine in Protein Denatured States. *Proc. Natl. Acad. Sci. U.S.A.* **2007**, *104* (8), 2661–2666.
- (92) Frishman, D.; Argos, P. Knowledge-Based Protein Secondary Structure Assignment. *Proteins* **1995**, *23* (4), 566–579.
- (93) Humphrey, W.; Dalke, A.; Schulten, K. VMD: Visual Molecular Dynamics. *J. Mol. Graphics* **1996**, *14* (1), 33–38.
- (94) Betancourt, M. R.; Thirumalai, D. Exploring the Kinetic Requirements for Enhancement of Protein Folding Rates in the GroEL Cavity. *J. Mol. Biol.* **1999**, *287* (3), 627–644.
- (95) Cheung, M. S.; Thirumalai, D. Nanopore–Protein Interactions Dramatically Alter Stability and Yield of the Native State in Restricted Spaces. *J. Mol. Biol.* **2006**, *357* (2), 632–643.
- (96) Ojeda, P.; Garcia, M. E.; Londono, A.; Chen, N. Y. Monte Carlo Simulations of Proteins in Cages: Influence of Confinement on the Stability of Intermediate States. *Biophys. J.* **2009**, *96* (3), 1076–1082.
- (97) Sigler, P. B.; Xu, Z. H.; Rye, H. S.; Burston, S. G.; Fenton, W. A.; Horwich, A. L. Structure and Function in GroEL-Mediated Protein Folding. *Annu. Rev. Biochem.* **1998**, *67*, 581–608.
- (98) Faeder, J.; Ladanyi, B. M. Molecular Dynamics Simulations of the Interior of Aqueous Reverse Micelles. *J. Phys. Chem. B* **2000**, *104* (5), 1033–1046.
- (99) Chimon, S.; Ishii, Y. Capturing Intermediate Structures of Alzheimer's Beta-Amyloid, Abeta(1–40), by Solid-State NMR Spectroscopy. *J. Am. Chem. Soc.* **2005**, *127* (39), 13472–13473.
- (100) Petkova, A. T.; Ishii, Y.; Balbach, J. J.; Antzutkin, O. N.; Leapman, R. D.; Delaglio, F.; Tycko, R. A Structural Model for Alzheimer's BetaAmyloid Fibrils Based on Experimental Constraints from Solid State NMR. *Proc. Natl. Acad. Sci. U.S.A.* **2002**, *99* (26), 16742–16747.
- (101) Antzutkin, O. N.; Leapman, R. D.; Balbach, J. J.; Tycko, R. Supramolecular Structural Constraints on Alzheimer's Beta-Amyloid Fibrils from Electron Microscopy and Solid-State Nuclear Magnetic Resonance. *Biochemistry* **2002**, *41* (51), 15436–15450.